Geomechanics and Engineering, *Vol. 27, No. 1 (2021) 75-85*
https://doi.org/10.12989/gae.2021.27.1.075

Mechanical model of lateral fracture for the overlying hard rock strata along coal mine goaf

Shankun Zhao[1, 2], Qiru Sui[1], Cong Cao[1], Xuecheng Wang[1], Chunlai Wang*[1], Daming Zhao[1], Yin Wang[1,2] and Yang Zhao[2]

[1]*School of Energy and Mining Engineering, China University of Mining and Technology Beijing, Ding 11, Xueyuan Road, Haidian District, Beijing, PR China*
[2]*Safety Technology Branch, CCTEG China Coal Research Institute, # 5, Qingniangoudong Road, Chaoyang District, Beijing, PR China*

(Received January 12, 2021, Revised August 6, 2021, Accepted September 29, 2021)

Abstract. Considering the continuous development of gob side entry driving technology, the influence of roof fracture on coal pillar is difficult to be accurately predicted. In order to explore the fracture structure characteristics of the overlying multi thick hard rock strata and its influence on coal pillars, the stress analysis tests of coal pillars under different roof fracture positions were designed. Different fracture positions of immediate roof and high-level thick hard rock were simulated by different corresponding positions of goaf, coal pillar edge line and rotary fixture line. According to four experimental design schemes, the strain distribution of coal mine goaf under different roof fracture combination positions was obtained. By analyzing the results of digital speckle pattern experiment, the distribution range and form of stress above coal pillar and low level thick hard rock are obtained, which provides theoretical basis for studying the whole process of coal pillar fracture.

Keywords: coal pillar; digital speckle; gob-side entry driving; roof fracture

1. Introduction

With the rapid development of economic construction, after decades of mining, a large number of coal mines have reached the end of mining. Due to the long-term mining, the coal resources are decreasing, and the resource mining is gradually transferred to the deeper ground.(Oge 2018, Xie *et al.* 2019, Milisavljevic *et al.* 2016) There is a large number of published studies (e.g., Waclawik *et al.* 2017, Wang *et al.* 2018, Wang *et al.* 2020a, b.) that describe that with the increase of mining depth, the large deformation of surrounding rock, rock burst, and coal and gas outburst caused by concentrated stress above coal pillars were becoming ever more hazardous. Previous research has established that the coal seam in the lower part of the mine is mined by means of roadway coal mining method, which results in a large number of cracks and subsidence areas in the upper part of the goaf. Roadway coal mining method is also called short column coal mining method. Within the section, every 10 to 30 meters, a horizontal and vertical crossroad is dug to cut the coal seam into many square, rectangular or diamond-shaped coal pillars with a length and width of 30 to 10 meters. Then the coal pillars are retrieved, and the roof of the mining area is left to collapse on its own. This method of coal mining is characterized by digging numerous lanes to form coal pillars, and then back mining the pillars. Gob-side entry driving with narrow coal pillars has been widely employed in China over the past several decades due to the particular stress environment and high resource recovery rate (Li *et al.* 2019). Coal pillars are reserved between two panels for separating the gob and maintaining the stability of the gob-side entry (Wattimena *et al.* 2013). Due to the influence of the overlying strata in the goaf on the stability of the surrounding rock of gob-side entry, there are still some tough problems, such as the high ground pressure, large deformation of the roadway surrounding rock, the unreasonable support technology (Song *et al.* 2016, Yang *et al.* 2017, Wang *et al.* 2018, Batugin *et al.* 2021). Many scholars have studied the fracture form of overlying rock in roadway driving along goaf. (Bai *et al.* 2015, Lee *et al.* 2020) The deformation law of gob side entry was studied, and its mechanical properties were analyzed. It was pointed out that there are “large and small structures” in the surrounding rock of gob side entry driving in fully mechanized top coal caving face, and the sustainability of large structure stability depends on the stability of small structure. Therefore, the mechanical model of large structure of overlying rock mass of roadway driving along goaf is established. Please *et al.* (2013) studied the problem of understanding how a coal mine roof collapses after secondary cutting of the supporting pillars to create small supporting snooks. Das *et al.* (2017) evaluated the influence of rock dip angle and coal seam dip angle on the stability of surrounding rock through the study of numerical simulation parameters. Han *et al.* (2008) used three-dimensional numerical simulation to study the influence of fault fracture zone on tunnel stability.

Some researchers have also carried out relevant researches and explorations on coal pillar (Jaiswal and Shrivastva 2008, Bertuzzi *et al.* 2016, Mathey and Van der Merwe 2016, Frith and Reed 2019). Based on a double-

*Corresponding author, Professor
E-mail: clwang@cumtb.edu.cn

ISSN: 2005-307X (Print), 2092-6219 (Online)

yield model for the gob materials and calibrated parameters, Jawed and Sinha (2018) studied the relationship between coal pillar width and the stability of roadway surrounding rock. Using the concept of constraint core and the three-dimensional stress distribution on the coal pillar, Das *et al.* (2019) deduced the strength calculation formulas of square, rectangular and super long coal pillars. Kumar *et al.* (2019) proposed a new method for simulating stress response of coal pillars using FLAC3D software. Gonza´lez-Nicieza *et al.* (2006) and Esterhuizen *et al.* (2011) developed an equation for estimating the pillar strength and selecting a safety factor. On the basis of the stress and displacement monitoring system, Esterhuizen *et al.* (2010) studied the relationship between roof fracture angle and gob side entry retaining stability. Coggan *et al.* (2012) studied the influence of roof lithology on roadway stability. On the basis of numerical simulation, Takashi *et al.* (2020) studied the relationship between pillar size and abutment pressure peak.

In addition, scholars also have done lots of works in aspects of theory research and materials fracture characteristics, etc (Kahraman *et al.* 2008, Vlahou and Worster 2015, Aliha and Bahmani 2017, Saadati *et al.* 2018, Bahmani *et al.* 2019, Kirmaci and Erkayaoglu 2020). These valuable works can provide some references for future study of rock fracture. Overall, lots of advanced techniques (i.e., SEM, and AE), theories and numerical methods are used to research the rock fracture characteristics under three-point bending loading condition, which shows the significance and necessity of obtaining the rock fracture characteristics.

The movement and failure mode of overburden determines the variation law of ground pressure, so it is necessary to study the lateral failure form and location of overburden. Different fracture position has influence on the fracture angle, stress and load distribution of coal pillar roof. In this paper, the whole process of stress state of coal pillar in different parts of high and low thickness hard rock fracture is studied by digital speckle method, and the influence of different roof fracture position on roof fracture angle and coal pillar is obtained.

2. Theoretical basis

2.1 Structural mechanics

There are four possible situations of the side breaking of the basic roof: breaking outside the roadway filling body; breaking above the filling body; breaking above the roadway; breaking above the solid coal. In order to study the main forms of roof breaking under the condition of thick immediate roof. The cantilever beam structural mechanical model is established when the basic roof is not broken (Fig. 1).

In the mechanical model, the force on the high-level thick and hard rock is divided into two stages. In the first stage, the supporting force on the high-level thick and hard rock is simplified as the concentrated load before the fracture of low-rise thick hard rock. In the second stage, the force on the high-level thick and hard rock is simplified as

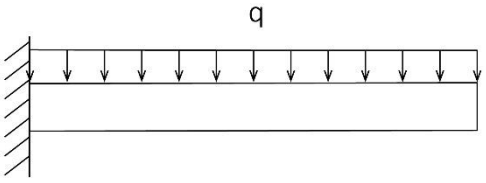

Fig. 1 Mechanical model of roof without fracture

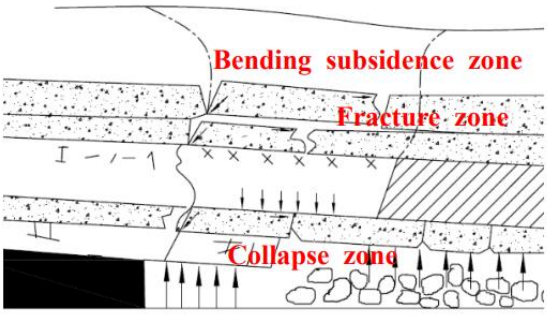

Fig. 2 Structural model of overlying strata of coal pillar in gob side entry

the uniform load in a certain range after the fracture of low-rise thick hard rock. From statics:

$$M = \int Ay\sigma dA \tag{1}$$

M is the bending moment and y is the distance from the calculated point to the neutral axis. By introducing Hooke's law into the above formula, we could further obtain:

$$M = \frac{E}{\rho}\int Ay^2\sigma d\varepsilon = \frac{EI}{\rho} \tag{2}$$

where σ is uniaxial stress, E is modulus of elasticity, ε is longitudinal linear strain,$\rho$is curvature. From the material mechanics, we could learn the rectangular section coefficient I of low thick hard rock and introduction of compensation coefficient χ , thus get:

$$M_u = \frac{\chi\sigma_c bh^3}{6} \tag{3}$$

2.2 Theory of thin plates

As shown in Fig. 2, during the mining process, the overlying strata will gradually form collapse zone, fracture zone and bending subsidence zone. In the mining area and both sides of the coal pillar, there will be the original rock stress area, the stress increase area, the stress decrease area and the stress stable area. The occurrence of concentrated stress will cause the failure and instability of the reserved coal pillar. This paper was mainly analyzed the influence of different positions of roof fracture on the force generated.

In the definition of elasticity, the plate is called a thin plate if the thickness of a plate is far less than the minimum size of the middle plane. The stress of the roof is simplified as a thin plate model and solved by Marcus algorithm.

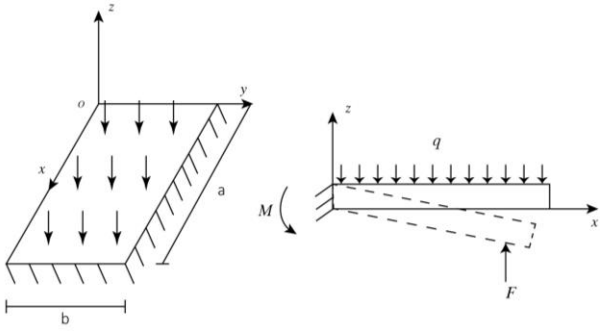

Fig. 3 Mechanical model of low stand thick hard rock

Compared with thick plate, thin plate theory is more conducive to the application of practical engineering problems.

There are three assumptions of thin plate bending

• Normal strain ε perpendicular to the middle plane ε_z. It could be ignored. Take $\varepsilon_z = 0$. From the equation $\frac{\partial \omega}{\partial z} = 0$, we get: $\omega = \omega(x, y)$.

• Stress component τ_{xz}, τ_{yz} and σ_z is much smaller than the other three components, and the deformation caused by them could be ignored.

• There is no displacement parallel to the middle plane of the thin plate.

According to the stress analysis of overlying strata, the rectangular coordinate system as shown in Fig. 3 is established. The force acting on the upper part of high-level thick and hard rock is simplified as q, and the transverse load q on the vertical median plane is $q_1 = q\cos\alpha$, longitudinal load q parallel to the median plane $q_2 = q\sin\alpha$. α is the fault subsidence angle of high-level thick hard rock. The width of the roof along the coal seam strike is a, the length along the coal seam dip is b, and the supporting force of the overlying strata to the roof is F.

Let the total deflection of low position thick and hard rock layer be ω, the deflection produced by q_1 is ω_1, the deflection produced by q_2 is ω_2, the deflection produced by F is ω_3.

The deflection differential equation of thin plate is as follows:

$$\nabla_\omega^4 = \frac{q(x,y)}{D} = f(x,y) \tag{4}$$

The elastic surface differential equation of thin plate under transverse load and longitudinal load is as follows:

$$D\nabla_\omega^4 = q_t + h\sigma_x\frac{\partial^2\omega}{\partial x^2} + h\sigma_y\frac{\partial^2\omega}{\partial y^2} + 2h\tau_{xy}\frac{\partial^2\omega}{\partial x\partial y} \tag{5}$$

where $D = \frac{E\delta^3}{12(1-\mu^2)}$ is the bending strength of the sheet, ∇ is the Laplace operator; ω is the deflection of thin plate, q_t is the normal load concentration, and $h\sigma_x$, $h\sigma_y$, $h\tau_{xy}$ is the internal force of thin surface.

The differential equation of ω is obtained:

$$D\nabla_{\omega_2}^4 = q_t + h\sigma_x\frac{\partial^2\omega_2}{\partial x^2} + h\sigma_y\frac{\partial^2\omega_2}{\partial y^2} + 2h\tau_{xy}\frac{\partial^2\omega_2}{\partial x\partial y} \tag{6}$$

where $q_t = q_{t1} + q_{t2} + q_{t3}$, $q_{t\phi} = h\sigma_x\frac{\partial^2\omega_\phi}{\partial x^2} + h\sigma_y\frac{\partial^2\omega_\phi}{\partial y^2} + 2h\tau_{xy}\frac{\partial^2\omega_\phi}{\partial x\partial y}$.

For the working face which has formed goaf and periodic weighting, the boundary conditions of roof are three fixed supports and one long simple support. The boundary conditions are as follows:

$$\left.\begin{aligned}(\omega)_{x=0} = 0, (\frac{\partial\omega}{\partial x}) = 0\\ (\omega)_{x=a} = 0, (\frac{\partial^2\omega}{\partial x^2}) = 0\\ (\omega)_{y=0} = 0, (\frac{\partial\omega}{\partial y}) = 0\\ (\omega)_{y=b} = 0, (\frac{\partial\omega}{\partial y}) = 0\end{aligned}\right\} \tag{7}$$

Take the following double trigonometric series to obtain the solution of double trigonometric series:

$$\omega = \sum_{m=1}^{\infty}\sum_{n=1}^{\infty} A_{mn}\sin^2\frac{m\pi x}{a}\sin^2\frac{n\pi y}{b} \tag{8}$$

where m and n are positive integers, all boundary conditions could be satisfied if the boundary conditions are brought in. The formula is introduced into the differential equation:

$$q_1 = \pi^4 D\sum_{m=1}^{\infty}\sum_{n=1}^{\infty}(\frac{3m^4}{a^4} + \frac{2m^2n^2}{a^2b^2} + \frac{3n^4}{b^4})A_{mn}\sin^2\frac{m\pi x}{a}\sin^2\frac{n\pi y}{b} \tag{9}$$

According to the expansion formula of Fourier series, the formula is as follows:

$$A_{mn} = \varepsilon\sum_{m=1}^{\infty}\int_0^a\int_0^b q_1\sin^2\frac{m\pi x}{a}\sin^2\frac{n\pi y}{b} \tag{10}$$

By introducing the above formula and comparing the coefficients, it is concluded that:

$$A_{mn} = \frac{\int_0^a\int_0^b q_1\sin^2\frac{m\pi x}{a}\sin^2\frac{n\pi y}{b}}{D\pi^4(\frac{3m^4}{a^4} + \frac{2m^2n^2}{a^2b^2} + \frac{3n^4}{b^4})} \tag{11}$$

In this model, the hydraulic cylinder is used to simulate the fracture process and location of high-level thick hard rock. Considering that the stress applied by high-level thick and hard rock is uniform load, which q_1 is a constant, the above formula could be rewritten as follows:

$$\begin{aligned}\int_0^a\int_0^b q_1\sin^2\frac{m\pi x}{a}\sin^2\frac{n\pi y}{b}dxdy &= q_1\int_0^a\sin^2\frac{m\pi x}{a}dx\int_0^b\sin^2\frac{n\pi y}{b}dy\\ &= \frac{q_1ab}{4mn\pi^2}\sin 2m\pi\sin 2n\pi\end{aligned} \tag{12}$$

By introducing Eq. (5), the expression of deflection is

obtained:

$$\omega_1 = \frac{qab\sin 2m\pi \sin 2n\pi \cos\alpha}{4Dmn\pi^6\left(\frac{3m^4}{a^4}+\frac{2m^2n^2}{a^2b^2}+\frac{3n^4}{b^4}\right)}\sum_{m=1}^{\infty}\sum_{n=1}^{\infty}\sin^2\frac{m\pi x}{a}\sin^2\frac{n\pi y}{b} \quad (13)$$

3. Mechanical model of lateral fracture of hard rock strata overlying coal pillars along goaf

After gob side entry excavation, the coal pillar not only moves to the side of the roadway affected by the roadway excavation, but also bulges out to the gob side coal wall under the influence of the lateral abutment pressure of the upper face. Both sides of the coal pillar have plastic deformation and failure. Taking the coal pillar within the height range of the roadway as the research object, the upper boundary of the coal pillar is the top coal, and the lower boundary is the roadway floor. Assuming that there is an elastic zone in the middle of coal pillar, the mechanical model of coal pillar side could be established as shown in the Fig. 4. The peak stress of roadway side in limit equilibrium zone of coal pillar is σ_{yt}, the peak stress of goaf side is σ_{yp}. According to the mechanical model of coal pillar side, the calculation model is established by taking coal pillar roadway side and goaf side as research objects.

According to the analysis of the edge stress of the side pillar of the roadway, the edge stress of the side pillar in the goaf is analyzed. One side is the solid coal in the coal pillar, and the other side is the top coal and caving coal body in the goaf side. The stress state of coal body edge is studied by the limit equilibrium, and the model is simplified and solved. The internal stress σ_y and width x_p of plastic zone at the edge of goaf is derived. The mechanical model and coordinate system are established as shown in the Fig. 5.

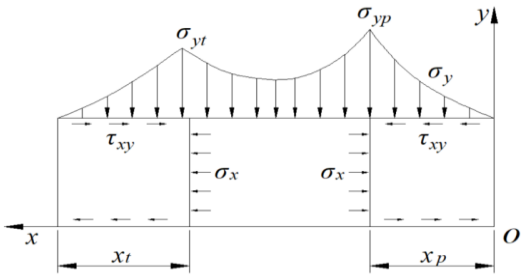

Fig. 4 Mechanical model of coal body at the edge of section pillar

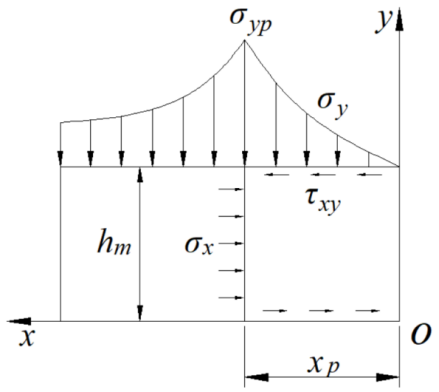

Fig. 5 Mechanical model of coal body at the side edge of goaf with section coal pillar

The equilibrium equation for solving the interfacial stress in the plastic zone is:

$$\left.\begin{aligned}\frac{\partial\sigma_y}{\partial x}+\frac{\partial\tau_{xy}}{\partial y}+X=0\\ \frac{\partial\sigma_y}{\partial y}+\frac{\partial\tau_{xy}}{\partial x}+Y=0\\ \tau_{xy}=-\left(c_0+\sigma_y\tan\varphi_0\right)\end{aligned}\right\} \quad (14)$$

The failure of coal body is caused by shear, and the failure satisfies Mohr-Coulomb criterion. At the limit strength of coal pillar, the boundary condition could be obtained:

$$\frac{\partial\sigma_y}{\partial y}-\frac{\partial\sigma_y}{\partial x}\tan\varphi_0+Y=0 \quad (15)$$

Suppose $\sigma_y = f(x)g(y)+A$. It could be obtained by substitution.

$$\frac{f'(x)}{f(x)}\tan\varphi_0=\frac{g'(x)}{g(y)}+Y \quad (16)$$

The two sides of the equation are only functions of X or Y, so the two sides of the equation are equal to the same constant B.

$$\frac{f'(x)}{f(x)}\tan\varphi_0=B \quad (17)$$

$$\frac{g'(x)}{g(y)}+Y=B \quad (18)$$

The solution could be obtained:

$$\left.\begin{aligned}f(x)=B_1e^{\frac{Bx}{\tan\varphi_0}}\\ g(y)=B_2e^{(B-Y)y}\end{aligned}\right\} \quad (19)$$

It could be obtained from the above formula:

$$\left.\begin{aligned}\sigma_y=B_0e^{(B-Y)y}e^{\frac{Bx}{\tan\varphi_0}}+A\\ \tau_{xy}=-\left[\left(B_0e^{(B-Y)y}e^{\frac{Bx}{\tan\varphi_0}}+A\right)\tan\varphi_0+C\right]\end{aligned}\right\} \quad (20)$$

where A and B_0 are undetermined constants, and $B_0 = B_1B_2$

Taking the whole plastic zone as the separation body, we could get the characteristic that the resultant force of X direction in the limit equilibrium zone is 0.

$$h_m\beta\sigma_y\big|_{x=x_p}-2\int_0^1\tau_{xy}\,dx=0 \quad (21)$$

Find the derivative of A and solve the problem:

$$\sigma_y\big|_{x=x_P}=Ce^{\frac{2\tan\varphi_0}{h_m\beta}x_P}-\frac{C_0}{\tan\varphi_0} \quad (22)$$

Let $x = x_P, y = y/2$ in equation (20), and compared with the above formula, we could get:

$$\left.\begin{aligned} A &= -\frac{C_0}{\tan\varphi_0} \\ B &= \frac{2\tan^2\varphi_0}{h_m\beta} \\ C = B_0 e^{\frac{(B-Y)}{2}h_m} &= B_0 e^{\frac{2\tan^2\varphi_0 - Yh_mB}{2\beta}} \end{aligned}\right\} \quad (23)$$

where $C = \frac{C_0}{tan\,\varphi_0}$, it could be deduced that:

$$B_0 = \left(\frac{C_0}{\tan\varphi_0}\right) e^{\frac{h_m\beta\gamma_0 - 2\tan^2\varphi_0}{2\beta}} \quad (24)$$

According to the conditions, the stress at any point in the limit equilibrium region is:

$$\begin{aligned} \sigma_y &= \left(\frac{C_0}{\tan\varphi_0}\right) e^{\frac{h_m\beta\gamma_0 - 2\tan^2\varphi_0}{2\beta} + \frac{2\tan\varphi_0}{h_m\beta}x + \left(\frac{2\tan^2\varphi_0}{2\beta} - \gamma_0\right)y} \\ \tau_{xy} &= -\left\{\left(\left(\frac{C_0}{\tan\varphi_0}\right) e^{\frac{h_m\beta\gamma_0 - 2\tan^2\varphi_0}{2\beta} + \frac{2\tan\varphi_0}{h_m\beta}x + \left(\frac{2\tan^2\varphi_0}{2\beta} - \gamma_0\right)y} \tan\varphi_0 + C_0\right)\right\} \end{aligned} \quad (25)$$

4. Results

4.1 Experimental materials

Coal samples and hard rock plates were collected from 3-1 coal seam, Bayan Gaole coal mine in Ordos City, Inner Mongolia Autonomous Region, the physical parameters of coal samples and hard rock plates are shown in the Table.1. In order to simulate the real mining process, before the experiment, tunnel excavation shall be carried out first for large coal samples. On account of the difficulty of rectangular tunnel excavation, the circular tunnel excavation is adopted in this mining. The diamond bit is used to drill and simulate the excavation and unloading of the tunnel. The high-strength electric drill is used to drill the face. The speed should be slow to prevent the mechanical damage of the coal samples. The location and size of the opening and the actual samples is shown in Fig. 6.

The coal sample processing equipment includes rock cutting machine, coring machine, radial drilling machine, grinding machine, etc. The processing steps of coal and rock samples include:

• Use a cutting machine to process the sample into a cube of about 150 mm × 150 mm × 150 mm;

• Fix the coal rock sample on the coring machine platform and drill through hole with diameter of 20^{+1}_{-1}mm with diamond bit;

• Grind the six ends of the coal pillar test piece on the grinder. After grinding, the non-parallelism of any two ends of the test piece shall not be greater than 0.05 mm, and the axial deviation shall not be greater than 0.25 °;

• When using high-strength electric drill to drill the working face, the speed shall be slow to prevent the mechanical damage of coal sample. Coal samples after processing as shown in Fig. 7.

According to the different fracture positions of the high-level and low-level thick and hard rocks, there are four

Table 1 The physical parameters of coal samples and hard rock plates

	Bulk apparent density (kg·m^{-3})	Elastic modulus (GPa)	Angle of internal friction (°)	Cohesion (MPa)	Poisson's ratio
Coal specimen	1299.15	2.845	18.52	13.894	0.281
Hard rock plates	2366.98	6.536	39.42	13.577	0.208

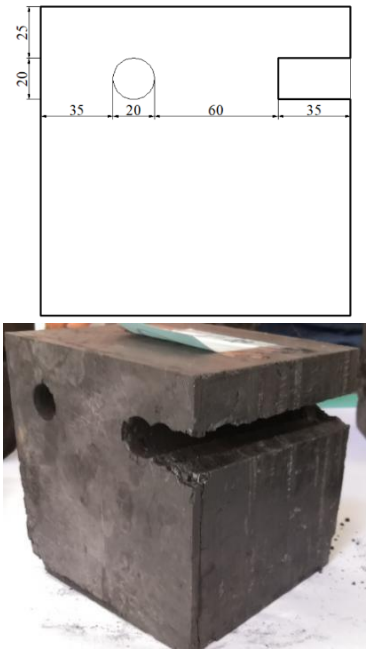

Fig.6 Specific excavation position and physical drawing of large coal sample

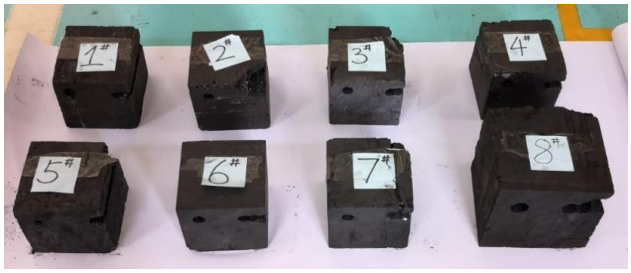

Fig.7 Coal samples after processing

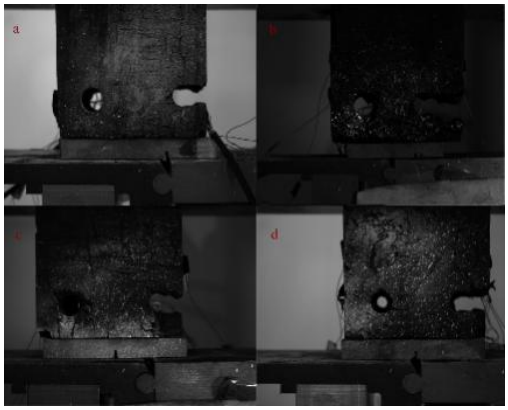

Fig. 8 Test diagram of four schemes (ABCD represents scheme I, II, III, IV)

schemes, as shown in Fig. 8. Scheme I: both the high-level and low-level thick and hard rock strata are fractured near the goaf side. Scheme II: the high-level thick and hard rock strata are fractured above the coal pillar and the low-level thick and hard rock strata are fractured near the goaf side. Scheme III: the high-level thick and hard rock strata are fractured near the goaf side and the low-level thick and hard rock strata are fractured above the coal pillar. Scheme IV: the high-level thick and hard rock strata and the lower thick and hard strata are all fractured above the coal pillar. In order to obtain more accurate test results, two samples are taken from each scheme for test.

4.2 Experimental setup

A testing machine and a non-contact whole field strain measuring system are used in the experiment. The loading system is an electro-hydraulic servo system controlled by computer with an accuracy of 1%. Matchid-3dhr, a non-contact full field strain measurement system of Institute of Physical and Chemical Technology of Chinese Academy of Sciences, is used to obtain the whole field strain data during the test, as shown in Fig. 9, including camera, lighting equipment and host. During the loading process, more than 1000 photos were taken, which covered the whole loading process.

During the preparation of test, the optical axis of CCD was perpendicular to the specimen surface and the light source kept stable for obtaining the images with steady gray values (Aliha *et al.* 2013, Jeong *et al.* 2016).

4.3 Experimental method

The test is divided into two steps, including static loading and lateral roof breaking. The specific operation of each step is as follows:

1) Add static load: Place the rotatable loading fixture on the operation platform. Put the jack in the clamping groove (the nozzle is outward), the jack is connected with the hand-held pressure pump, and fixed with flexible materials around to prevent the equipment dumping. The prepared square coal sample is placed on the upper part of the fixture. The parallel loading steel plate is placed on the top of the sample, and loaded by the pressure testing machine.

2) Side broken roof: After the coal sample is loaded, pressurize it at a constant speed through the jack. Record the pressure value of the dial in time. Through the rotation of the steel plate, the coal sample is pressurized, forcing the side hanging roof to break. Record the fracture position and relevant monitoring data.

4.4 2D DIC Theory

The non-contact whole field deformation measurement system mainly adopts 2D DIC method. Combined with industrial close-range shooting technology, the industrial camera is used to collect real-time digital images of various deformation stages of objects. The digital image correlation algorithm is used to match deformation points on the surface of objects, and the coordinates of matching points are reconstructed.

Fig. 9 Non-contact whole field strain measurement system

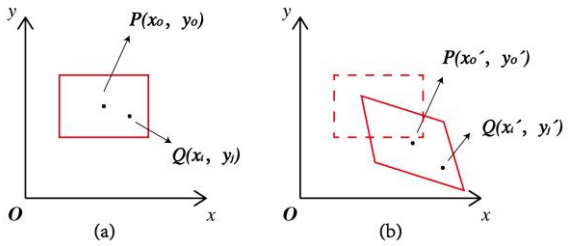

Fig. 10 Schematic of subset before and after deformation (a) Reference image and (b) Deformed image

2D DIC obtains the displacement of pixels by tracking the change of gray distribution of digital image. In order to avoid the same gray distribution in the image, the random distribution of speckle is usually taken as the shooting object, and charge coupled device (CCD) camera is used to record the reference image of the former state and the deformation image of the latter state.

Fig. 10 shows the distribution before and after the deformation, where Oxy is the coordinate system. In order to calculate the displacement of point $P(x_0, y_0)$, as shown in Fig. 10(a), select a reference subset of circle or rectangle (shown by red rectangle box) within a certain range around point $P(x_0, y_0)$, $Q(x_i, y_j)$ is any point in the reference subset, i and j represent column coordinates and row coordinates of point Q in the subset respectively. As shown in Fig. 10(b), after the graph is deformed, $Q(x_i, y_j)$ becomes $Q'(x_i', y_j')$. The target subset centred on the point $P'(x_0', y_0')$ could be described by the first order shape function.

$$x_i' = x_i + u + u_x \Delta x + u_y \Delta y \tag{26}$$

$$y_j' = y_j + v + v_x \Delta x + v_y \Delta y \tag{27}$$

where u and v are the displacements of $P(x_0, y_0)$ in x and y directions respectively; u_x, u_y, v_x, v_y are the first-order differential of displacement; Δx and Δy are the coordinate differences between any point $Q(x_i, y_j)$ and the central point $P(x_0, y_0)$ in the reference subset respectively. For the sub-pixel points in the target subset, a specific interpolation algorithm is used to get the gray value. The similarity between the reference subset and the variant subset could be evaluated by the correlation criterion. The target subset with the highest similarity to the reference subset could be found in the deformation graph, that is, the

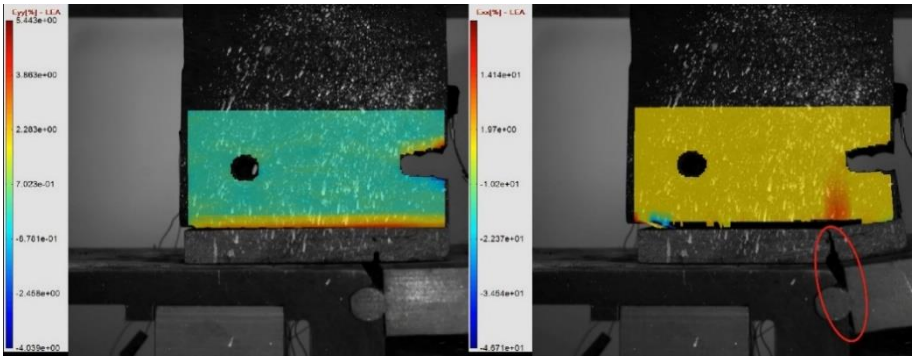

Fig. 11 Scheme 1 strain nephogram

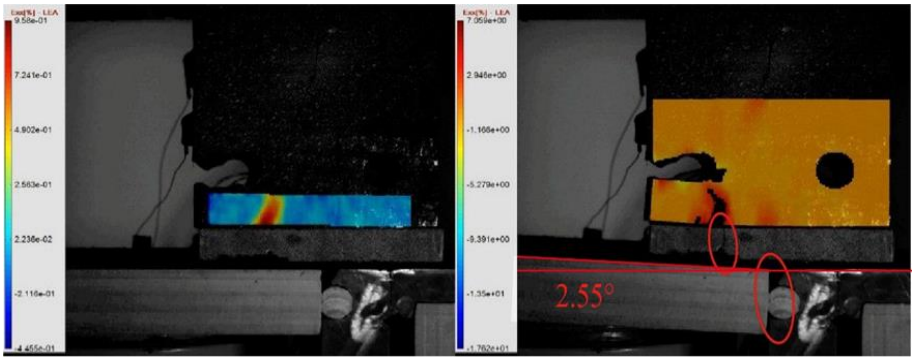

Fig. 12 Scheme 2 strain nephogram

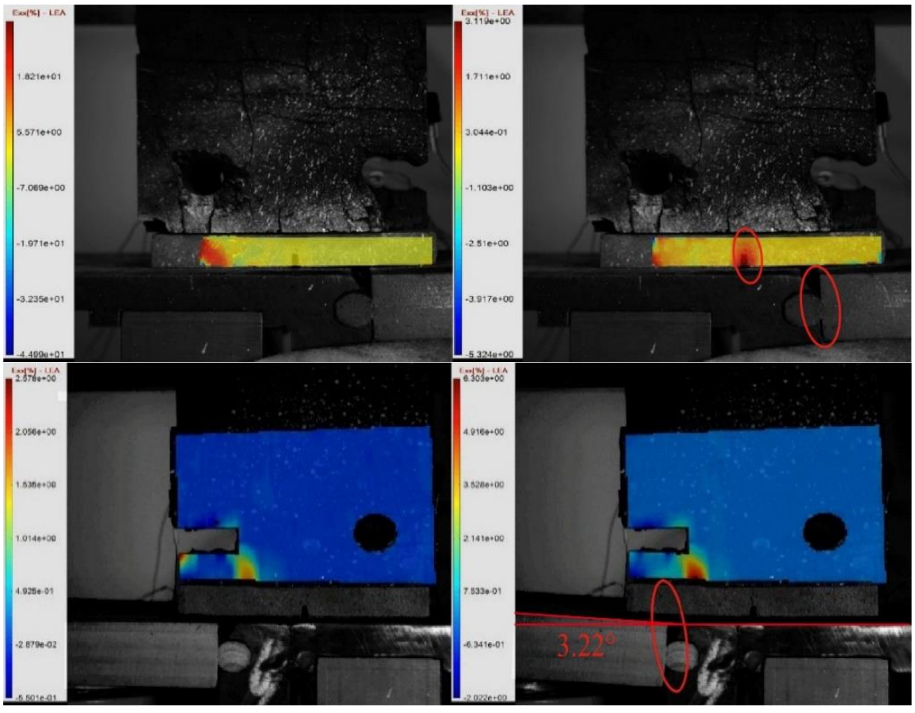

Fig.13 Scheme 3 strain nephogram

P' point corresponding to the point P could be found, so as to determine the displacement u and v of the point P. At present, the sub-pixel displacement calculation accuracy of 2D DIC could reach 0.01 pixel. In this study, the open-source 2D DIC application program Ncorr (Blaber *et al.* 2015) is used to calculate the displacement of speckle.

The purpose of this study is to analyze the influence of different roof fracture positions on roof fracture angle and coal pillar. Therefore, the position and form of different forces are produced by controlling the broken position of roof strata. At the same time, the yield and pressure redistributions of coal pillar are considered. In the experimental results, we could intuitively understand the strain distribution and change process. By observing the

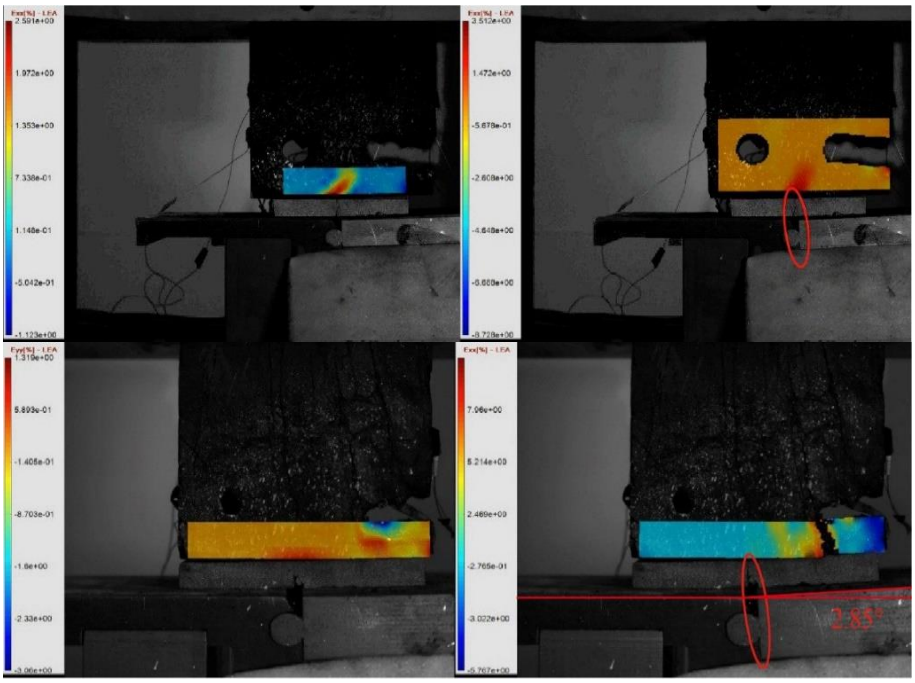

Fig. 14 Scheme 4 strain nephogram

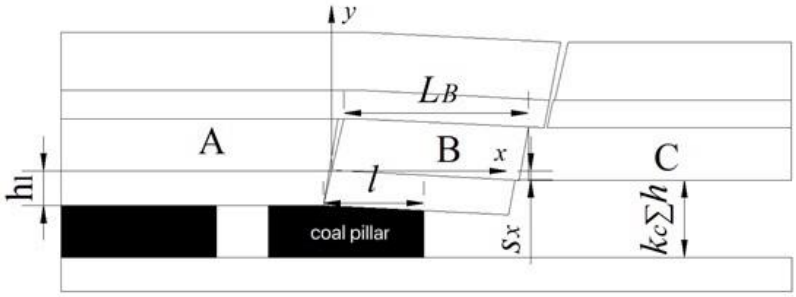

Fig. 15 Mechanical model of lateral structure of overlying hard rock strata in gob side entry

distribution of different colors in the diagram (Figs. 11-14), the strain size at different positions could be determined. In the stress nephogram, the stress magnitude is represented by the color. As the color changes from red to blue color, the stress value changes from positive to negative values. The corresponding values are specified in the picture.

Comparison scheme 1 and scheme 2: the low level thick hard rock layer is fractured at the edge of coal pillar, and the high level thick hard rock layer is fractured at different positions. In the early stage of scheme II, the coal pillar of scheme II is different from that of scheme I. The stress concentration in the goaf area near the coal pillar appears quickly, which is shown as red yellow bright strip. The strain zone does not distribute vertically, but inclines to the coal pillar and its position migrates to the coal pillar. At the same time, the phenomenon of strain increase appears above the coal pillar, which shows that the pressure of the overlying roof is also borne above the coal pillar. During the test, scheme 2 also shows that the coal pillar bears more pressure from the overlying roof. When the goaf roof collapses, the pressure exerted on the lower strata in scheme II is also greater.

Comparison scheme 1 and scheme 3: the high level thick hard rock layer is located near the goaf side, and the fracture position of the low level thick hard rock layer is different. In the early stage of the experiment, the roof dip angle is large, the strain concentration area is transferred to the top of the coal pillar. The Red Spot appears at the position of the prefabricated crack, and the low-level thick hard rock layer finally breaks here. The stress of coal pillar and goaf edge is relatively uniform, and there is no obvious strain concentration area. In scheme 1, with the experiment, the stress begins to concentrate on the side of the goaf, and the plastic zone also concentrates on the side of the goaf near the coal pillar. The high-level strata begin to become thick and hard in one side. There is no strain increase above the coal pillar, and the stress is uniform and stable.

Comparison scheme 2 and scheme 4: the high position thick hard rock layer breaks above the coal pillar, and the low position thick hard rock layer fracture position is different. Both of them have the phenomenon of stress concentration above the coal pillar. The strain area is not vertical distribution, but inclined to one side of the goaf, The stress concentration at the edge of the goaf. When the roof of goaf collapses, the pressure exerted by them on the lower strata is greater.

Comparison scheme 3 and scheme 4: the low level thick hard rock layer breaks above the coal pillar, and the high level thick hard rock layer breaks at different positions. In scheme 4, the stress concentration appears above the coal pillar, and the strain area is not vertically distributed, but inclines to one side of the goaf. At the same time, the phenomenon of stress concentration also appears at the edge of the goaf. With the increase of dip angle of high-level thick hard rock stratum, the side of coal pillar close to goaf is still under the pressure of roof. When the roof of goaf collapses, the pressure on the lower strata is greater.

It is known from the above that the coal pillar should be depressurized according to scheme 3. The high level thick hard rock is easy to fracture in roadway, and the rotary block formed after fracture is long, which has a strong control effect on low level thick and hard rock. The low position thick hard rock could not resist the rotation subsidence of the roof, and could only passively bear the severe pressure caused by the subsidence of the high-level thick and hard rock during the compression process. The occurrence position of low position thick hard rock stratum, that is, the height of low position thick hard rock layer, has an important influence on the weighting strength of stope. The height of the low position thick hard rock layer corresponds to the thickness of the direct roof rock layer. The thicker direct roof strata collapse and fall behind could fully fill the goaf, leaving less movement space for the fault block, and the weighting strength is relatively gentle.

According to the mechanical model shown in Fig. 15., the rotation subsidence S_x of key block B at different positions X.

σ_x is used to represent the compressive stress at different horizontal distances from the base point of the fault, the compressive deformation Δh_x of the low stand thick and hard rock could be written as:

$$\Delta h_x = \frac{\sigma_x h_m}{E} + \frac{\sigma_x h_1}{E_1} \tag{28}$$

Among them, h_1 and h_m are the thickness of immediate roof and coal seam respectively; E and E_1 represent the elastic modulus of coal pillar and direct roof respectively.

The low position thick and hard rock could not prevent the given deformation of the high position thick and hard rock layer, and the immediate roof could not control the rotation of the low level thick and hard rock layer. Therefore, there is $S_x = \Delta h_x$, and the compressive stress σ_X on the coal pillar could be obtained as follows.

$$\sigma_x = \frac{[h_m - (k_c - 1)h_1]x}{\left(\frac{h_m}{E} + \frac{h_1}{E_1}\right) L_B \cos\phi} \tag{29}$$

In the case of scheme 3, the ultimate strength of coal pillar is σ_y, which means that the coal pillar is damaged, and the maximum load borne by coal pillar shall not be greater than its strength limit.

$$\sigma_x = \frac{[h_m - (k_c - 1)h_1]x}{\left(\frac{h_m}{E} + \frac{h_1}{E_1}\right) L_B \cos\phi} \leq \sigma_y \tag{30}$$

5. Conclusions

Through four different fracture location schemes, the whole process of stress state of coal pillar in different parts of high and low thickness hard rock fracture is analyzed. The influence of different roof fracture position on coal pillar is obtained. The main conclusions are as follows：

• When the fracture position of the low level thick hard rock is the same the high level thick hard rock fracture position is above the coal pillar, the stress concentration phenomenon above the coal pillar is obvious. The strain area is not vertical distribution, but inclines to both sides. When the roof of goaf collapses, the pressure on the lower strata is greater.

• When the fracture position of high-level hard rock is close to the side of goaf, the influence of fracture position of low level thick hard rock on coal pillar is obvious. When the low level thick and hard rock fracture is on the edge of the goaf, the stress begins to concentrate to one side of the goaf, and the plastic area also concentrates on the side near the coal pillar. When the low level thick hard rock fracture is above the coal pillar, the stress on the coal pillar and the edge of the goaf is relatively uniform, and there is no obvious strain concentration area. The dip angle of high-level thick hard rock began to increase. There is no strain increase above the coal pillar. Moreover, the stress is uniform and stable.

• When the fracture position of high level thick hard rock is above the coal pillar, the influence of the fracture position of low level thick hard rock on coal pillar is weak. The results show that the stress concentration above the coal pillar and the strain area are not vertical distribution. It is inclined to one side of the goaf, and the stress concentration occurs at the edge of the goaf. When the roof of goaf collapses, the pressure exerted by them on the lower strata is greater.

• The mechanical model of coal body at the side of goaf and side of roadway of coal pillar is established. The edge stress of coal pillar is deduced. The calculation model of ultimate strength of coal pillar under different broken position state of roof is solved, and the instability criterion of coal pillar is obtained.

• The cracks in the coal samples were increased and enlarged during the fabrication of the experimental specimens, and the effect of these cracks on the coal samples was difficult to control. The method of theory to realize the fracture location of the roof in engineering experiments needs further study. The future research direction should optimize the roof fracture model and further determine the roof fracture criterion.

Acknowledgments

This work was jointly supported by the National Natural Science Foundation of China (Grant No. 52074294), the National Key Research and Development Project (Grant No. 2017YFC0804201, 2017YFC0804203).

References

Aliha, M.R.M. and Bahmani, A. (2017), "Rock fracture toughness study under mixed mode I/III loading", *Rock Mech. Rock Eng.*, **50**(7), 1-13. http://doi.org/10.1007/s00603-017-1201-7.

Aliha, M.R.M., Hosseinpour, G.R. and Ayatollahi, M.R. (2013), "Application of cracked triangular specimen subjected to three-point bending for investigating fracture behavior of rock materials.", *Rock Mech. Rock Eng.*, **46**(5), 1023-1034. http://doi.org/10.1007/s00603-012-0325-z

Bahmani, B., Abedi, R. and Clarke, P.L. (2019), "A stochastic bulk damage model based on Mohr-Coulomb failure criterion for dynamic rock fracture", *Appl. Sci.*, **9**(5), 830. http://doi.org/10.3390/app9050830.

Bai, J.B., Shen, W.L., Guo, G.L., Wang, X.Y. and Yu, Y. (2015). "Roof deformation, failure characteristics, and preventive techniques of gob-side entry driving heading adjacent to the advancing working face", *Rock Mech. Rock Eng.*, **48**(6), 2447-2458. http://doi.org/10.1007/s00603-015-0713-2.

Batugin, A., Wang, Z., Su, Z. and Sidikovna, S.S. (2021), "Combined support mechanism of rock bolts and anchor cables for adjacent roadways in the external staggered split-level panel layout", *Int. J. Coal Sci. Technol.*, **3**, 1-15. http://doi.org/10.1007/s40789-020-00399-w.

Bertuzzi, R., Douglas, K. and Mostyn, G. (2016), "An approach to model the strength of coal pillars", *Int. J. Rock Mech. Min. Sci.*, **100**(89), 165-175. http://doi.org/10.1016/j.ijrmms.2016.09.003

Blaber, J., Adair, B. and Antoniou, A. (2015), "Ncorr: Open-source 2D digital image correlation Matlab software", *Exp. Mech.*, **55**(6), 1105-1122. http://doi.org/10.1007/s11340-015-0009-1.

Coggan, J., Gao, F., Stead, D. and Elmo, D. (2012), "Numerical modelling of the effects of weak immediate roof lithology on coal mine roadway stability", *Int. J. Coal Geol.*, **90**, 100-109. http://doi.org/10.1016/j.coal.2011.11.003.

Das, A.J., Mandal, P.K., Bhattacharjee, R., Tiwari, S., Kushwaha, A. and Roy, L.B. (2017), "Evaluation of stability of underground workings for exploitation of an inclined coal seam by the ubiquitous joint model", *Int. J. Rock Mech. Min. Sci.*, **93**, 101-114. http://doi.org/10.1016/j.ijrmms.2017.01.012.

Das, A.J., Mandal, P.K., Paul, P.S. and Sinha, P.K. (2019), "Generalised analytical models for the strength of the inclined as well as the flat coal pillars using rock mass failure criterion", *Rock Mech. Rock Eng.*, **52**(10), 3921-3946. http://doi.org/10.1007/s00603-019-01788-7.

Esterhuizen, E., Mark, C., Engineer, P.R., Engineer, M. and Murphy, M.M. (2010), "Numerical model calibration for simulating coal pillars, gob and overburden response", *Proceedings of the 29th International Conference on Ground Control in Mining*, Morgantown, West Virginia, U.S.A., July.

Esterhuizen, G.S., Dolinar, D.R. and Ellenberger, J.L. (2011), "Pillar strength in underground stone mines in the United States." *Int. J. Rock Mech. Min. Sci.*, **48**(1), 42-50. http://doi.org/10.1016/j.ijrmms.2010.06.003

Frith, R. and Reed, G. (2019), "Limitations and potential design risks when applying empirically derived coal pillar strength equations to real-life mine stability problems", *Int. J. Min. Sci. Technol.*, **27**(1), 17-25. http://doi.org/10.1016/j.ijmst.2018.11.024.

González-Nicieza, C., Álvarez-Fernández, M.I., Menéndez-Díaz, A. and Alvarez-Vigil, A.E. (2006), "A comparative analysis of pillar design methods and its application to marble mines", *Rock Mech. Rock Eng.*, **39**(5), 421-444. http://doi.org/10.1007/s00603-005-0078-z.

Han, K.C., Ryu, D.W., Kim, S.K. and Bae, K.C. (2008), "Stability analysis of the spillway tunnel located on the granite region including fault fractured zone", *Tunn. Undergr. Sp.*, **18**(1), 58-68. http://doi.org/KJD:ART001246745

Jaiswal, A. and Shrivastva, B.K. (2008), "Numerical simulation of coal pillar strength", *Int. J. Rock Mech. Min. Sci.*, **46**(4), 779-788. http://doi.org/10.1016/j.ijrmms.2008.11.003.

Jawed, M. and Sinha, R.K. (2018), "Design of rhombus coal pillars and support for roadway stability and mechanizing loading of face coal using SDLs in a steeply inclined thin coal seam—a technical feasibility study.", *Arab. J. Geosci.*, **11**(15), 1-14. http://doi.org/10.1007/s12517-018-3747-4.

Jeong, J.U., Choi, J.B., Huh, N.S. and Kim, Y.J. (2016), "Stress intensity factor and elastic crack opening displacement solutions of complex cracks in pipe using elastic finite-element analyses", *J. Pressure Vessel Technol.*, **138**(1). http://doi.org/10.1115/1.4031128.

Kahraman, S., Soylemez, M. and Fener, M. (2008), "Determination of fracture depth of rock blocks from P-wave velocity", *B. Eng. Geol. Environ.*, **67**(1), 11-16. http://doi.org/10.1007/s10064-007-0110-5.

Kirmaci, A. and Erkayaoglu, M. (2020), "Thermographic analysis of failure for different rock types under uniaxial loading.", *Geomech. Eng.*, **23**(6), 503-512. http://doi.org/10.12989/gae.2020.23.6.503.

Kumar, A., Waclawik, P., Singh, R., Sam, S. and Korbel, J. (2019), "Per-formance of a coal pillar at deeper cover: Field and simulation studies", *Int. J. Rock Mech. Min. Sci.*, **113**, 322-332. http://doi.org/10.1016/j.ijrmms.2018.10.006.

Lee, H., Oh, T.M. and Park, C. (2020), "Analysis of permeability in rock fracture with effective stress at deep depth", *Geomech. Eng.*, **22**(5), 375-384. http://doi.org/10.12989/gae.2020.22.5.375

Li, X.Y., Zhang, N., Liang, D.X. and Zhao, Y.M. (2019), "Study on efficient utilization technology of coal pillar based on gob-side entry driving in a coal mine with great depth and high production", *Sustainability*, **11**(6), 1706. http://doi.org/10.3390/su11061706.

Mathey, M. and Van der Merwe, J.N. (2016), "Critique of the South African squat coal pillar strength formula", *J. S. Afr. I. Min. Metall.*, **116**(3), 291-299. http://doi.org/10.17159/2411-9717/2016/v116n3a11.

Milisavljevic, V., Tosic, D., Cokorilo, V. and Ristovic, I. (2016), "Modelling of AT rockbolts parameters for "Soko" underground coal mine.", *Tehnicki vjesnik*. http://doi.org/10.17559/TV-20140825132622.

Oge, I.F. (2018), "Prediction of top coal cavability character of a deep coal mine by empirical and numerical methods", *J. Min. Sci.*, **54**(5), 793-803. http://doi.org/10.1134/S1062739118054903.

Please, C.P., Mason, D.P., Khalique, C.M., Ngnotchouye, J.M.T., Hutchinson, A.J., Van, M.J.N. and Yilmaz, H. (2013), "Fracturing of an Euler–Bernoulli beam in coal mine pillar extraction.", *Int. J. Rock Mech. Min. Sci.*, **64**, 132-138. http://doi.org/10.1016/j.ijrmms.2013.08.001.

Saadati, M., Forquin, P., Weddfelt, K., Larsson, P.L. and Hild, F. (2018), "On the mechanical behavior of granite material with particular emphasis on the influence from pre-existing cracks and defects", *J. Test. Eval.*, **46**(1), 33-45. http://doi.org/10.1520/JTE20160072.

Sasaoka, T., Mao, P., Shimada, H., Hamanaka, A. and Oya, J. (2020), "Numerical analysis of longwall gate-entry stability under weak geological condition: A case study of an Indonesian coal mine", *Energies*, **13**(18). http://doi.org/10.3390/en13184710.

Song, W.J., Qiao, W.J., Vladimir, V.P., Wu, D.H. and Li, Y.Z. "Research on the support technology of bolt and cable in deep high stress roadway", *Proceedings of the Russian-Chinese Symposium* "*Coal in Century: Mining, Proceesing, Safety*, Kemerovo, Russia, October.

Vlahou, I. and Worster, M.G. (2015), "Freeze fracturing of elastic porous media: A mathematical model.", *Proc. Royal Soc. A*

Math. Phys. Eng. Sci., **471**, 2175. http://doi.org/10.1098/rspa.2014.0741.

Waclawik, P., Kukutsch, R., Konicek, P., Ptacek, J., Kajzar, V., Jan, N., Stas, L., Soucek, K. and Vavro, M. (2017), "Stress state monitoring in the surroundings of the roadway ahead of longwall mining." *Procedia Eng.*, **191**, 560-567. http://doi.org/10.1016/j.proeng.2017.05.218.

Wang, C.L., Chen, Z., Liao, Z.F., Hou, X.L., Li, H.T., Wang, A.W., Li, C.F., Qian, P.F., Li, G.Y. and Lu, H. (2020), "Experimental investigation on predicting precursory changes in entropy for dominant frequency of rockburst.", *J. Cent. South Univ.*, **27**, 2834-2848. http://doi.org/10.1007/s11771-020-4506-8.

Wang C.L., Hou, X.L. and Liu, Y.B. (2020), "Three-dimensional crack recognition by unsupervised machine learning", *Rock Mech. Rock Eng.*, **54**(2), 893-903. http://doi.org/10.1007/s00603-020-02287-w.

Wang, Q., He, M.C., Yang, J., Gao, H.K., Jiang, B. and Yu, H.C. (2018), "Study of a no-pillar mining technique with automatically formed gob-side entry retaining for longwall mining in coal mines.", *Int J Rock Mech Min Sci.*, **110**, 1–8. http://doi.org/10.1016/j.ijrmms.2018.07.005

Wattimena, R.K., Kramadibrata, S., Sidi, I.D. and Azizi, M.A. (2013), "Developing coal pillar stability chart using logistic regression", *Int. J. Rock Mech. Min. Sci.*, **58**, 55-60. http://doi.org/10.1016/j.ijrmms.2012.09.004,

Xie, H.P., Gao, M.Z., Zhang, R., Peng, G.Y., Wang, W.Y. and Li, A.Q. (2019), "Study on the mechanical properties and mechanical response of coal mining at 1000 m or deeper", *Rock Mech. Rock Eng.*, **52**(5), 1-16. http://doi.org/10.1007/s00603-018-1509-y.

Yang, D.W., Ma, Z.G., Qi, F.Z., Gong, P. and Zhang, R.R. (2017), "Optimizati on study on roof break direction of gob-side entry retaining by roof break and filling in thick-layer soft rock layer", *Geomech. Eng.*, **13**(2), 195-215. http://doi.org/10.12989/gae.2017.13.2.195.

CC